Journal of Materials Research and Technology 28 (2024) 3186–3195

Contents lists available at ScienceDirect

Journal of Materials Research and Technology

journal homepage: www.elsevier.com/locate/jmrt

Influence of building directions on the impact properties of NiTi fabricated via laser powder bed fusion

Xiao-Long Zhang [a,c], Shuo Wang [b], Yue Jiang [a], Jie Huang [c], Shu-Peng Wang [a,**], Qing-Quan Zhang [a], Qiang Li [a], Yu-Qing Guo [a], Zhi-Hui Zhang [a,*]

[a] Key Laboratory of Bionic Engineering, Ministry of Education, Jilin University, Changchun, 130022, China
[b] Luoyang Ship Material Research Institute, Luoyang, 471023, China
[c] Department of Mechanical Engineering, University College London, WC1E 7JE, UK

ARTICLE INFO

Handling editor: L Murr

Keywords:
Charpy impact test
NiTi shape memory alloys
Laser powder bed fusion
Building directions
Impact toughness

ABSTRACT

The Charpy impact toughness is a crucial mechanical parameter in the application of materials within the realm of engineering. This study represents the pioneering investigation into the influence of different building directions on the Charpy impact toughness of NiTi shape memory alloys (SMAs) produced via laser powder bed fusion (LPBF). Texture analysis reveals that C0 and C90 exhibit a pronounced <001>// building direction (BA), while C45 demonstrates a strong texture along <110> and <111>. The impact test results demonstrate that C0 exhibits superior impact toughness with an absorbed energy of 12.87 J. The fractured surfaces are examined using the scanning electron microscope (SEM) and transmission electron microscope (TEM). Among them, the electron backscatter diffraction (EBSD) results indicate that the samples with higher geometrically necessary dislocation (GND) and kernel average misorientation (KAM) values can effectively reflect superior impact toughness. In contrast, fewer high-angle grain boundaries (HAGBs) are preferable. Due to the adiabatic effect, the phase transformation of the samples from austenite to martensite doesn't appear under the impact loading. Additionally, this paper discusses the impact of texture orientation, defects, and the relationship between loading direction and deposited layers on the impact toughness of the samples. These findings on impact properties would provide valuable guidance for engineering applications of NiTi SMAs.

1. Introduction

As one of the most attractive functional materials, NiTi SMAs [1] have a special phase transformation process under changing external conditions, which leads to the unique shape memory effect or the superelastic effect. Additionally, NiTi SMAs also exhibit excellent mechanical properties, corrosion resistance [2], fatigue resistance [3], and high damping [4]. Due to these outstanding characteristics, NiTi SMAs have been widely applied in aerospace [5], civil engineering [6], and other engineering fields [7,8]. In these applications, many structures fabricated using the NiTi SMAs may experience impact or high-strain rate loads during the explosion and crash circumstances. Therefore, the ability of structural components to withstand sudden stress is a critical parameter as it directly influences the product's service life, safety, and reliability [9]. Hence, it's necessary to investigate the impact properties of NiTi SMAs.

In recent decades, many studies have explored the energy absorption ability and failure mechanical behaviors of the NiTi SMAs under impact loading. Cui et al. [10] studied the dynamic impact fracture behaviors of the NiTi SMAs using a split Hopkinson compression bar. Wang et al. [11] examined the impact fracture behavior of NiTi SMAs on the drop-weight impact system. These studies found that both impact energy and the environment temperature have an important effect on the impact resistance of NiTi SMAs. Additionally, laser shock experiments and driven flyer plates were also used to investigate the impact resistance behaviors of NiTi SMAs, as reported in Refs. [12,13]. However, Charpy impact tests with a strain rate in the range of 10^2-10^3 s^{-1} have not been employed for investigating the impact properties of NiTi SMAs. Furthermore, most of the NiTi SMAs (NiTi wires [14], NiTi plates [11], and bar [10]) used to study the impact properties above were made by the traditional processing technology.

As widely acknowledged, traditional NiTi SMAs have poor

* Corresponding author.
** Corresponding author.
E-mail addresses: wsp@jlu.edu.cn (S.-P. Wang), zhzh@jlu.edu.cn (Z.-H. Zhang).

https://doi.org/10.1016/j.jmrt.2023.12.160
Received 7 November 2023; Received in revised form 18 December 2023; Accepted 18 December 2023
Available online 23 December 2023

Table 1
Chemical composition of the NiTi powder (wt%).

Element(wt.%)	Ni	Fe	C	O	N	Ti
Powders	55.8	0.0083	0.0066	0.0576	0.0067	Bal.

machinability, severely limiting their application space [15]. As a layer-by-layer approach for creating desired shapes, LPBF can produce complex parts rapidly, which has injected new vitality into the development of NiTi SMAs [16,17]. Therefore, LPBFed NiTi SMAs are in great demand for aerospace and civil engineering [5,6]. Nevertheless, the NiTi SMAs may undergo complex thermal processes during the LPBF processing. Specifically, when the laser traverses a layer of powder, rapid melting and solidification occur with high efficiency. Subsequently, as the laser moves through the upper layer, the lower powder experiences cyclic reheating due to temperature gradients from above, resulting in non-uniform heat distribution across the LPBFed part. Consequently, this phenomenon significantly influences both microstructure and texture [18]. As a result, the properties of NiTi SMAs are influenced, particularly when altering the building direction which can further modify the velocity of solid/liquid interface and thermal conditions [19]. Currently, many studies have studied this aspect.

Specifically, Moghaddam et al. [20] found that the 0° samples exhibited the highest ultimate strength and elongation in the tensile test. While in the compression behavior, Mohammadreza et al. [21] reported

Table 2
Phase transition temperatures of C0, C45 and C90 (°C).

Sample	A_s	A_f	M_s	M_f	M_p	A_p
C0	−4.3	26.1	8.3	−35.1	−11.8	11.5
C45	−7.2	30.3	15.5	−40.1	−9.5	13.2
C90	−13.1	37.6	24.7	−53.2	−10.1	13.1

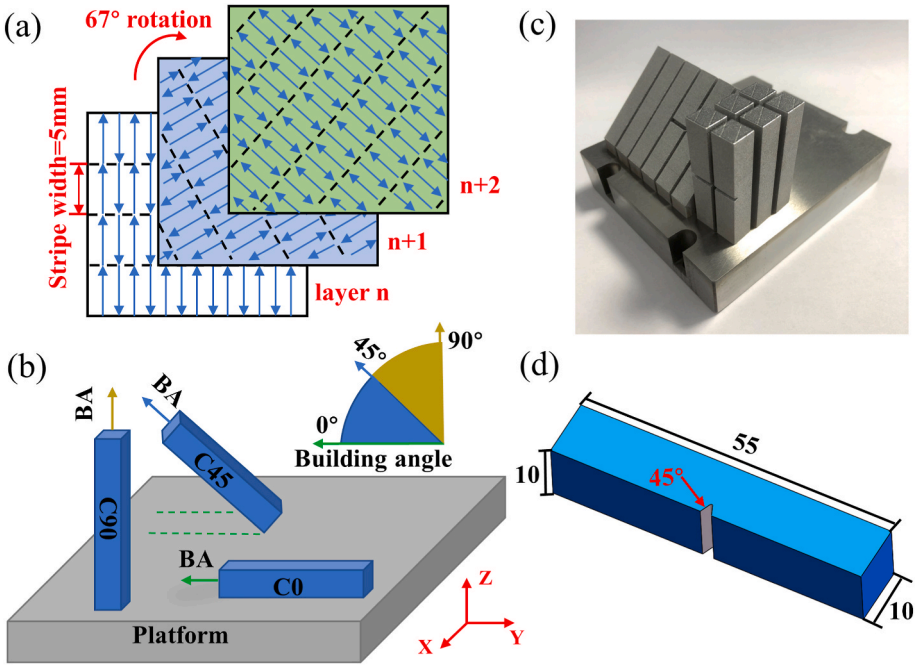

Fig. 1. Schematic of (a) the stripe rotation scanning strategy, (b) LPBFed impact samples with the different building angle (BA), referred to as C0, C45, and C90, respectively, and (d) the impact samples after wire-cut; (c) Actual view of the impact samples.

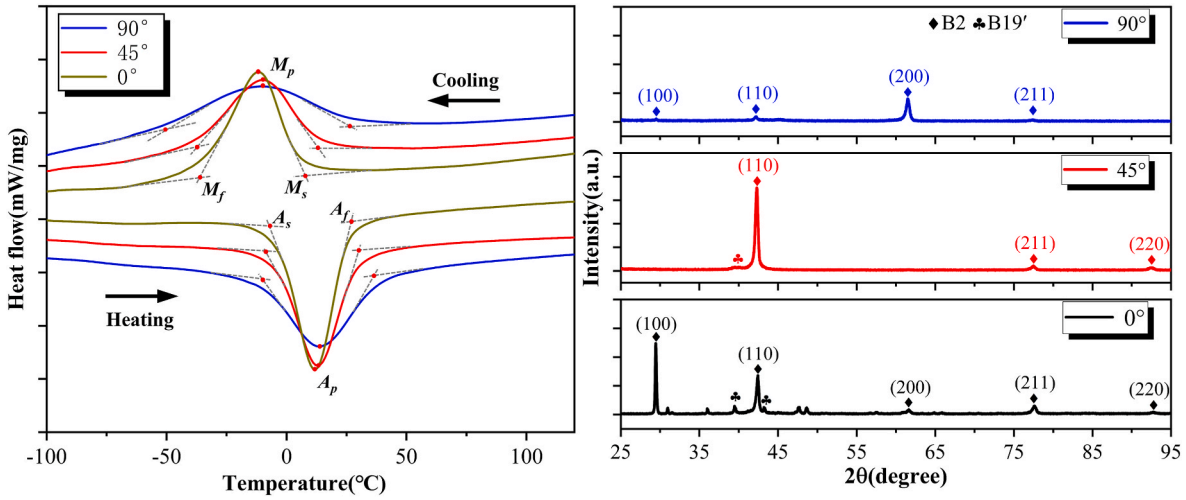

Fig. 2. (a) DSC curves of different samples; (b) XRD results of C0, C45, and C90.

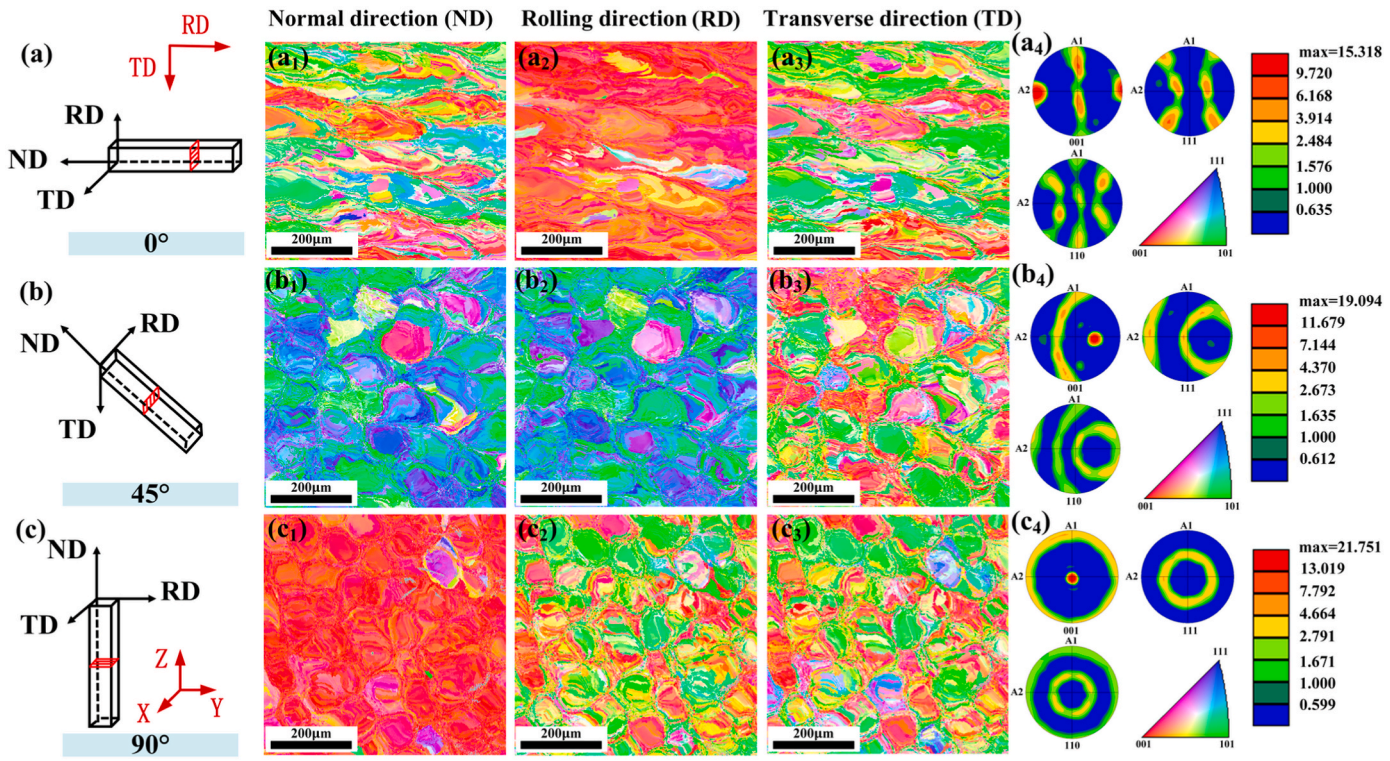

Fig. 3. The schematic diagram of the information acquisition surface marked with red color: (a) C0, (b) C45, and (c) C90; IPFs (Normal direction (ND), Rolling direction (RD) and Transverse direction (TD)) of (a_1) (a_2) (a_3) C0, (b_1) (b_2) (b_3) C45 and (c_1) (c_2) (c_3) C90; IFs of (a_4) C0, (b_4) C45 and (c_4) C90.

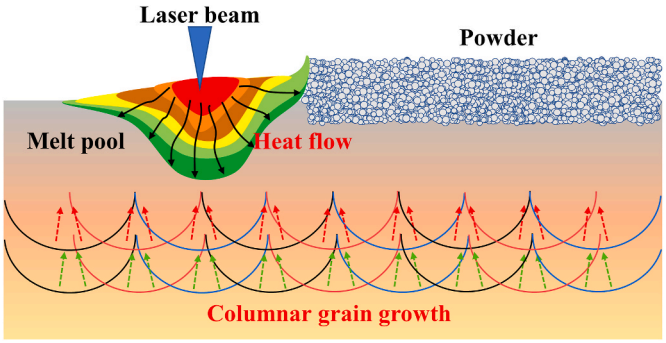

Fig. 4. The schematic diagram of the melt pool and the grain growth orientation.

that the 45° sample demonstrated the earliest failure. However, the 45° sample showed the highest fatigue life in Ref. [22]. According to the analysis results, texture could be the main influencing factor. Interestingly, Safaei et al. [23] proved that the 90° sample showed the best strength and ductility in torsional behavior compared to the 0° and 45° samples. As seen, all the studies above focus on the influence of the building direction on the tensile, compression, torsional, and fatigue behaviors. However, the relationship between the Charpy impact toughness and the building direction is unclear. Therefore, it is necessary to investigate the influence of the building direction on the impact properties of the LPBFed NiTi SMAs.

In this paper, we address the research gap regarding the impact properties of LPBFed NiTi SMAs tested by the Charpy impact tester at a strain rate of 10^2-$10^3 s^{-1}$. We investigate the influence of three different building directions (0°, 45°, and 90°) on the impact properties of LPBFed NiTi SMAs. Specifically, we meticulously analyze the load-displacement curves obtained from the Charpy impact testing machine. Secondly, we carefully observe the impact fracture surface and cross-section using SEM and EBSD techniques. Furthermore, we conduct a comprehensive analysis including texture orientation, defects, and their relationship with loading direction and deposited layers to explore how building directions affect the impact properties of NiTi SMAs.

2. Experimental procedures

2.1. Materials and samples

The NiTi powder (55.8 wt% Ni) produced with the electrode induction-melting gas atomization (EIGA) technique (Shenzhen Minatech Co Ltd.) was used in this work, which is the same as that used in our previous work [24]. The powder has a spherical or near-spherical morphology with 15–53 μm dimension, and the chemical composition is shown in Table 1. The experimental samples are manufactured by the SLM machine (BLT S210) equipped with a Yb-fiber laser with a maximum power of 500 W. During the forming process, the stripe rotation scanning strategy presented in Fig. 1 (a) is employed. The stripe width is 5 mm. The hatch rotation angle is 67° between the adjacent layers. The hatching spacing is 80 μm and the layer thickness is 30 μm. The detailed parameters to produce the impact samples with LPBF were reported in our early work [24]. The samples were printed under an argon atmosphere with less than 20 ppm oxygen content.

The impact samples are fabricated with the building direction of 0°, 45°, and 90° concerning the NiTi platform, referred to as C0, C45, and C90, respectively (Fig. 1 (b)). Fig. 1 (c) shows the actual photos of the impact samples. According to ASTM standard E23-12c, the dimensions of impact specimens with a 45° notch is 50 mm (length) × 10 mm (width) × 10 mm (height), and the notch size is 2 mm (Fig. 1 (d)).

2.2. Thermomechanical characterization and impact test

The differential scanning calorimetry (DSC) method is performed to evaluate the transformation temperatures of the samples with different building directions using a Netzsch DSC214, German. The weight of DSC

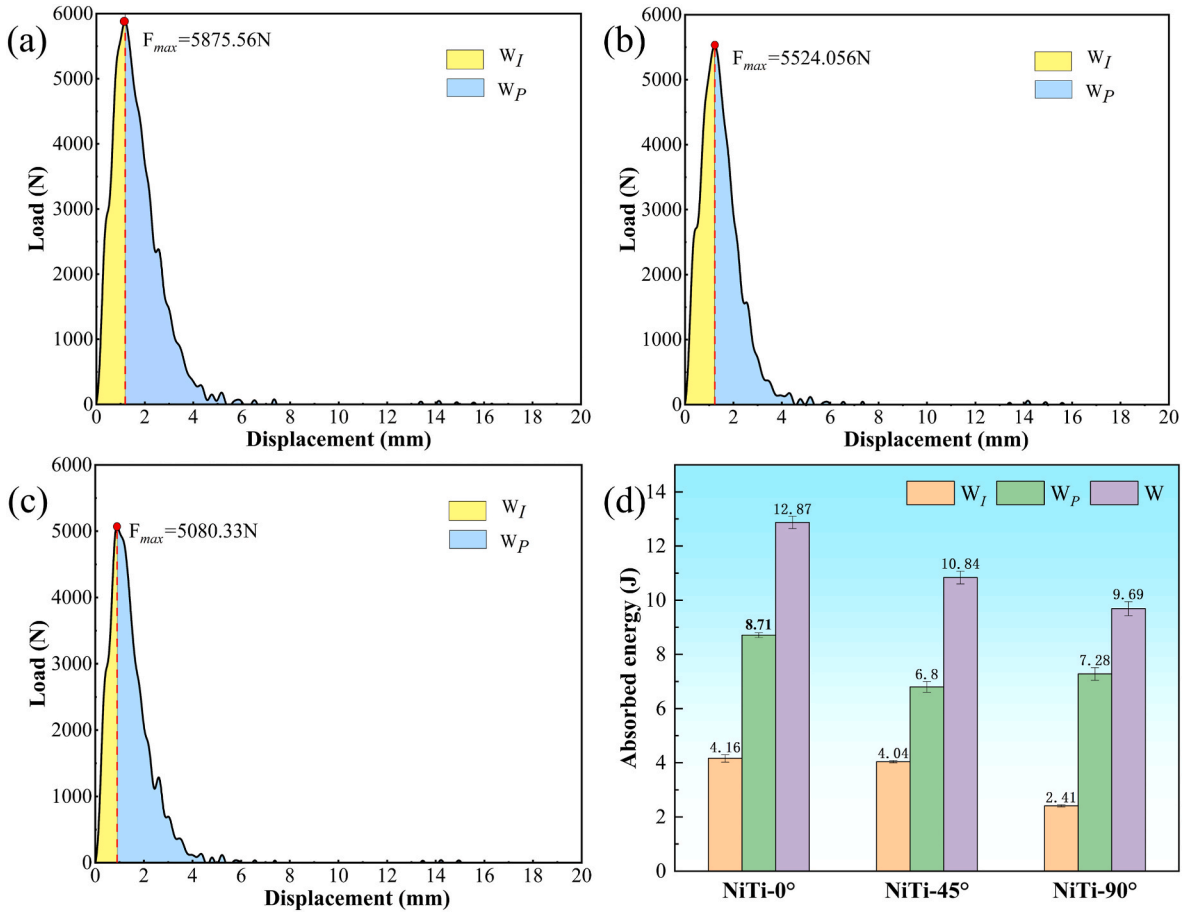

Fig. 5. Load-displacement curves of (a) C0, (b) C45, (c) C90; (d) The total impact absorbed energy (W), crack initiation energy (W_I), and crack propagation energy (W_p) of C0, C45, and C90.

specimens is about 10 mg and the heating/cooling rate is 10 °C·min^{-1} from −150 °C to 120 °C. To ensure repeatability, three DSC specimens have been tested for each sample with different building directions. The analysis of the phase structure is performed using X-ray diffraction (XRD, DX-2700BH, China) with the Cu Kα radiation. The scanning angle ranges from 25° to 95° with a scanning rate of 2°·min^{-1}.

The impact test is performed on a standard Charpy impact machine (MTS Exceed E22, the strain rate is 10^2-10^3 s^{-1} [25]) following the ISO 148–1:2016 standard. The result of the impact absorbed energy is an average of three values obtained from the three specimens with the same parameters at room temperature. The impact absorbed energy of each tested specimen is shown in Table S1.

2.3. Microstructure characterization

The microstructure investigation of the NiTi impact samples is performed on the cross-section parallel to the loading direction and the cross-section perpendicular to the fracture surface of the impact samples. All the specimens are ground using silicon carbide paper with 600 mesh–2000 mesh and then polished with the diamond particle suspension. Finally, the specimens need to be etched using the etchant solution of CH3OH: HNO3 = 4:1. Further microstructural assessments are performed by the SEM (FEI Scios2, USA). SEM also examines the morphology of the impact fracture surfaces. Crystallographic orientation information for each sample is collected using EBSD.

Specimen disks for TEM are ground to a thickness of 50 μm and then electro-polished using a twin-jet thinning electropolishing device and an electrolyte consisting of 25 % HNO_3 in methanol at 243 K and 30 V. The TEM analysis is performed in a JEM-2100 at an acceleration voltage of 200 KV.

3. Results and discussion

3.1. Transformation behavior

Fig. 2 (a) shows the results of the DSC measurements for the samples with different building directions. All the samples show a single-step transformation with a slight change in transformation temperatures (TTs), including martensite peak temperature (M_p), martensite start temperature (M_s), martensite finish temperature (M_f), austenite peak temperature (A_p), austenite start temperature (A_s) and austenite finish temperature (A_f). Table 2 lists the corresponding TTs.

As shown in Fig. 2 (a), the martensite transformation start temperature is below room temperature (25 °C) for all the samples. Furthermore, as the building directions of the samples change from 0° to 90°, the transformation peaks become wider, while the position of the transformation peaks remain essentially unaffected. There is no significant connection between the building directions and the TTs. Generally speaking, the TTs are sensitive to the LPBF process parameters, e.g., the laser powder, scanning speed, and hatch space. The changes in these parameters could affect the TTs utilizing their influence on the proportion of Ni atoms and the microstructure of the samples [26–28]. However, as all samples are manufactured using similar laser parameters [24] in this work, the proportion of the Ni atoms and the microstructure would not change significantly, and thus no obvious changes in the TTs are observed. It was worth noting from Fig. 2 (a) and Table 2 that the C90 has a wider martensite transformation peak than the C0 and C45. This suggests a complicated effect of the thermal histories, which could

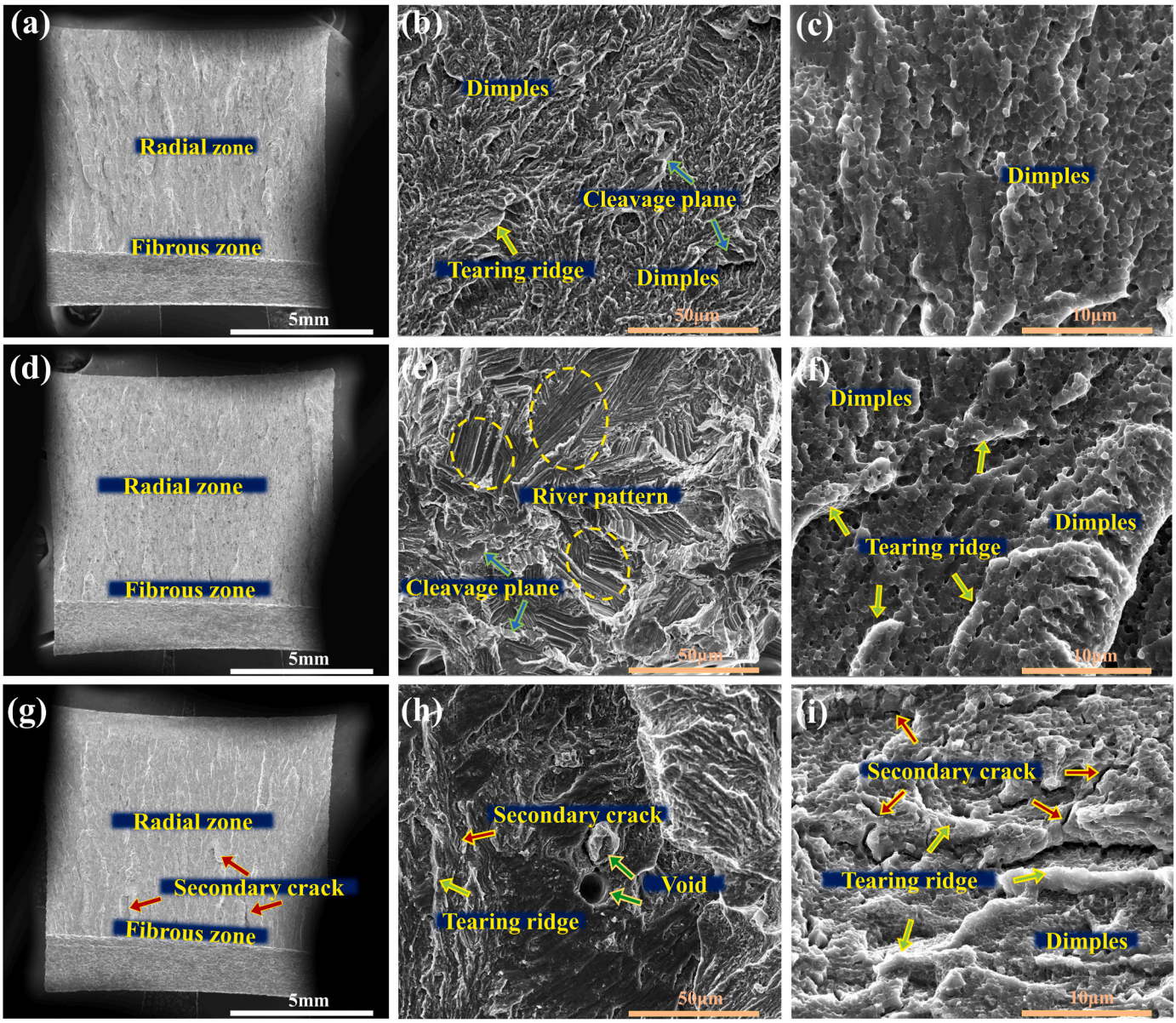

Fig. 6. Fractography of (a–c) C0, (d–f) C45, and (g–i) C90: (a) (d) (g) overall morphology, (b) (e) (h) high magnification SEM photo of the fibrous zone, (c) (f) (i) higher magnification SEM photo of the radial zone.

produce different effects on the formation of the non-uniform microstructure, the presence of residual stress, and the pick-up of oxides, nitrides, or other impurities [29–32]. On the other hand, the higher numbers of layers of the C90 could enhance the effect of the thermal histories, thereby broadening the peak of the martensite transformation. As described in Refs. [28,33], the width of the martensite transformation peak could be effectively alleviated by heat treatment.

Fig. 2 (b) shows the XRD results of C0, C45, and C90 at room temperature. As shown, the B2 austenite phase dominates in the three samples at room temperature, and no other secondary phases were detected. Such results are consistent with the results of the DSC in Fig. 2 (a). However, the peak intensity has a slight difference. Among them, the main reflection plane of C0 and C90 is the (100) plane, and the main reflection plane of the C45 is the (110) plane. It has been reported [34] that this difference may arise from the variation in the crystallographic texture orientations caused by the different building directions [21]. This effect of the building directions will be analyzed in section 3.3.

3.2. Microstructural analysis

The microstructure analyses of C0, C45, and C90 are analyzed on the cross-section surface (10 × 10) and the surface perpendicular to the loading directions, respectively. Fig. 3 shows the inverse pole figure (IPF) and pole figure (PF) obtained by the EBSD analysis. As shown in Fig. 3 (a_1), the C0 exhibits the large columnar grains along the building direction. As shown in Fig. 3 (b_1) and (c_1), the C45 and C90 show large grains with chessboard patterns and a high number of sub-grains distributed at the boundaries of the large grains, respectively. The columnar grain morphology observed in the C0 arises from the high cooling rate during the LPBF processing [35].

Fig. 4 depicts a schematic representation of the formation process of columnar grains, elucidating their structural characteristics and growth mechanisms. As shown, a molten pool forms when the laser melts the powder. In the molten pool, heat flow radiates from the center of the laser spot to the surroundings. The high thermal gradient could provide a high driving force for solidification. During the solidification, the grains may grow towards the center of the molten pool and along the

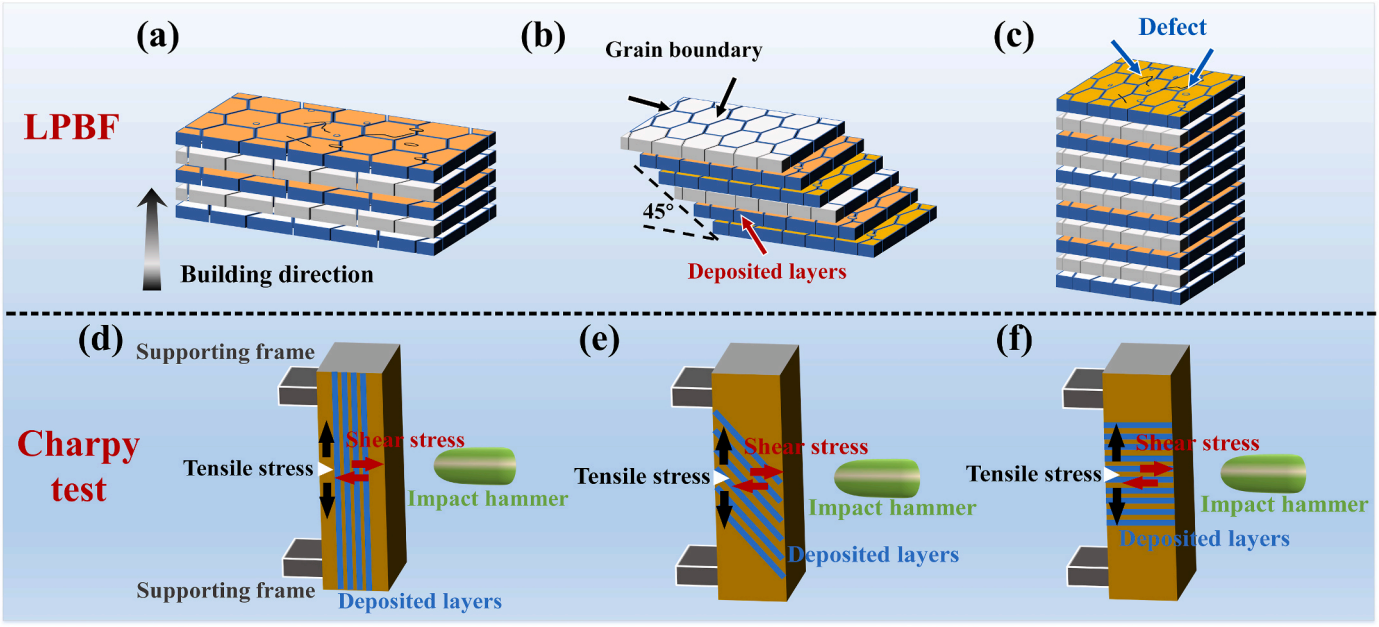

Fig. 7. The schematic of the forming process: (a) C0, (b) C45, (c) C90, and the Charpy impact test: (d) C0, (e) C45, and (f) C90.

highest thermal gradient as shown by the dotted line. Based on the layer-by-layer additively building technology, the processes of the rapid heating and cooling and the multiple remelting could result in the overgrowth of the grains along the deposition direction across multiple layers and hence the formation of the columnar grain morphology [36, 37].

It can be seen from Fig. 3 (a_2) that the IPF of the C0 along the RD exhibits a strong texture of <001>//RD. This strong texture in the C0 can be attributed to the parallel alignment between BD and RD (Fig. 3 (a)). Similar observations have been reported in previous researches [34,38,39]. In contrast, the C45 shows a crystallographic texture of <111>+<110>//ND or RD and <110>//TD (Fig. 3 (a_1-a_3)), which is consistent with the XRD results in Fig. 2 (b). The EBSD analyses of the C45 performed on the cross-section are located at 45° concerning the deposition direction, thus the C45 exhibits the different preferred orientations. However, according to the PF of the C45, the {001} pole appears 45° away from the center of the projection plane along the TD direction, which indicates that the crystal lattice of the C45 had been tilted 45°. Essentially, the {001} of the C45 still grows parallel to the deposition direction. Along the ND (Fig. 3 (c_1)), the C90 shows an obvious <100>//ND texture. It could be concluded from the above results that all the samples have the same <100> texture toward the deposition direction, but different textures toward the building direction. These differences in the types of textures will lead to distinct thermomechanical properties among the three types of samples examined in this work.

3.3. Impact properties

Fig. 5 shows the load-displacement curves of the C0, C45, and C90 samples obtained in our impact tests. The maximum load point (F_{max}) on these load-displacement curves can be used to divide the total impact absorbed energy (W) into two components: the crack initiation energy (W_I) and the crack propagation energy (W_P). W_I and W_P reflect the abilities to resist the crack initiation and subsequent propagation, respectively, corresponding to the areas under the load-displacement curves represented by yellow and blue regions [40–42]. Fig. 5 (d) summarizes the difference in W, W_I, and W_P among the C0, C45, and C90 samples. As shown, W_I values of the C0, C45, and C90 were 4.16 J, 4.04 J, and 2.41 J, respectively indicating that both C0 and C45 exhibit stronger resistance to the crack initiation compared to C90. It should be noted from Fig. 5 that W_P values for C0, C45, and C90 are 8.17 J, 6.80 J, and 7.28 J, respectively. These values are higher than the respective W_I values by 209 %, 168 %, and 302 %. This suggests that a majority of the impact-absorbed energy is utilized for driving the crack propagation during the impact processing. The total impact absorbed energies of the C0, C45, and C90 are 12.87 J, 10.84 J, and 9.69 J, respectively. This indicates that the C0 exhibits the highest impact toughness among these three samples.

Fig. 6 shows the SEM fracture surface morphologies of the C0, C45, and C90, which can be used to investigate the fracture mechanism. As shown in Fig. 6 (a) (d) and (g), a relatively flat macroscopic fracture surface is observed, encompassing the radial zone (crack propagation region) located in the middle of the fracture surface and the fibrous zone (crack initiation region) near the V-notch. The shear lip (final fracture region) also could not be observed. It is apparent that all three samples exhibit low-impact energy levels insufficient for shear lip formation. The magnified fracture surface morphologies in Fig. 6 (b)(c), (e)(f), and (h)(i) show that there are significant differences in the fracture surface morphologies among C0, C45, and C90. As shown in Fig. 6 (b)(c), the stress distribution on C0 appears to be homogeneous, and it exhibits clear quasi-cleavage fracture characteristics, including substantially larger dimples, small-sized tearing ridges, and cleavage planes. By comparison, the fracture surface of C45 exhibits many “river patterns”, large-sized tearing ridges, and cleavage planes (Fig. 6 (d)). These characteristics are shown as brittle fracture features. Similarly, the fracture surface of C90 also exhibits brittle fracture characteristics including many large-sized tearing ridges, voids (Fig. 6 (h)), and secondary cracks (Fig. 6 (h)(i)) as well, which cause the impact energy of C90 to dissipate. These observations suggest that compared to both C45 and C90, C0 demonstrates superior crack propagation resistance capabilities consistent with its higher W value.

As mentioned in section 3.1, given that the used laser processing parameters were the same for C0, C45, and C90 samples, it could be inferred that the structure and the type of defects in each deposition layer would also exhibit similarities. Therefore, the significant disparities in their W values may arise from the relationship between the loading direction and the building direction, as well as the forming height that potentially contribute to differences in defect quantities. As shown in Fig. 7 (a–c), C90 has the maximum forming height from the

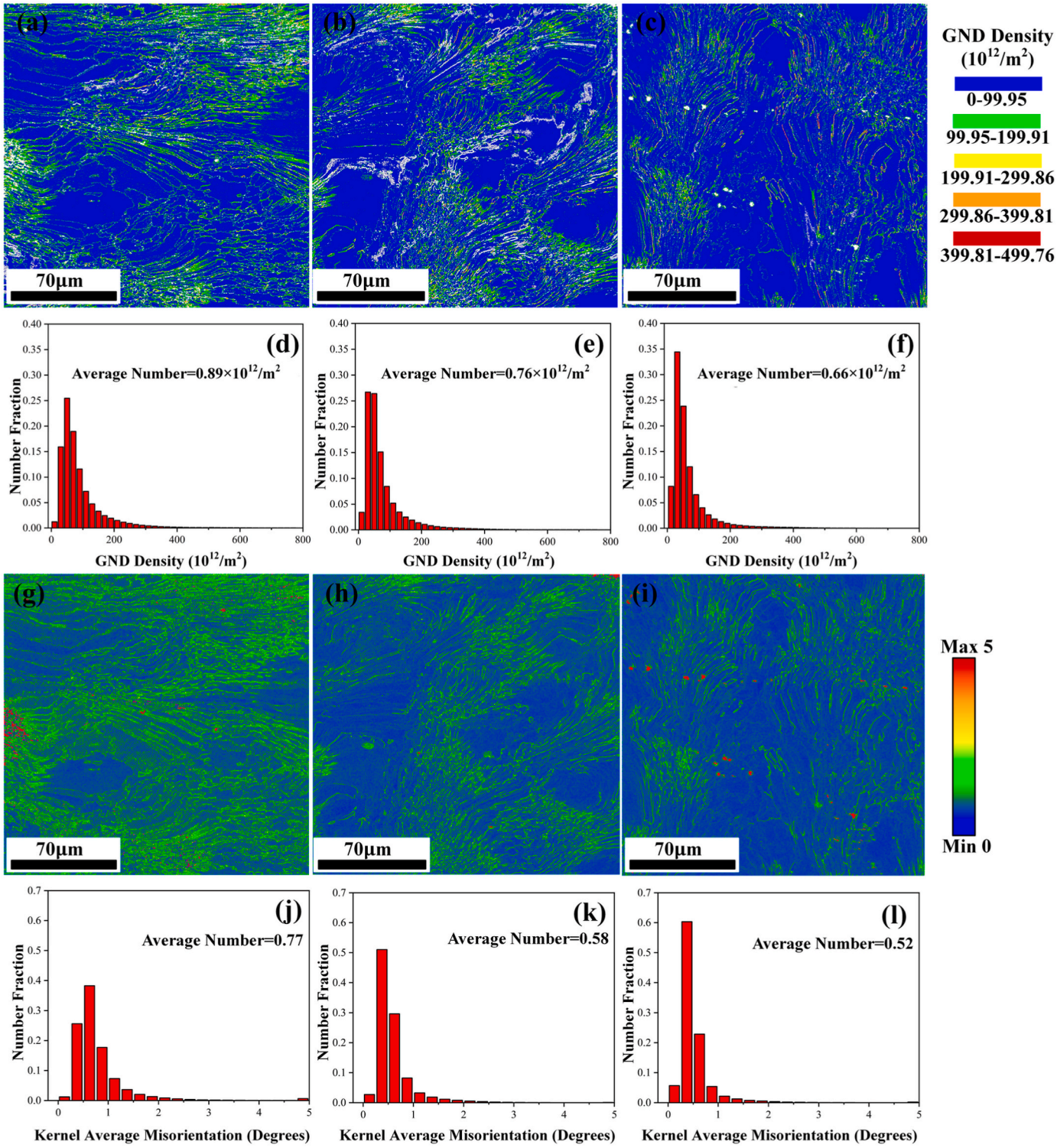

Fig. 8. The distributions of GND density of (a) C0, (b) C45, and (c) C90; GND density statistics of (d) C0, (e) C45, and (f) C90; KAM maps of (g) C0, (h) C45 and (i) C90; KAM statistics of (j) C0, (k) C45 and (l) C90.

bottom, which increases the possibility of the effect of the defects on the interface between two deposited layers, e.g., un-melted areas, micro-cracks, and air pores. These defects may lead to a higher possibility of the stress concentration in C90 than in the other samples, thereby facilitating crack initiation and propagation [43]. In addition, the relative position of the interlayer interface concerning the loading direction has a significant effect on the impact properties [19,43,44]. Fig. 7 (a–c) schematically illustrate the spatial arrangement of the deposited layers, and Fig. 7 (d–f) demonstrate the position relationship between the interlayer interface of the deposited layers and the loading direction. Specifically, it can be observed that the loading directions are parallel, perpendicular, or at 45° to the interlayer interface of C90, C0, and C45, respectively. As shown in Fig. 7 (f), the interlayer interface in C90 exhibits a parallel orientation to the loading direction, which may potentially result in the easier failure of the interlayer bonding, and lead to the fracture subsequently. Therefore, C90 shows a weaker impact resistance

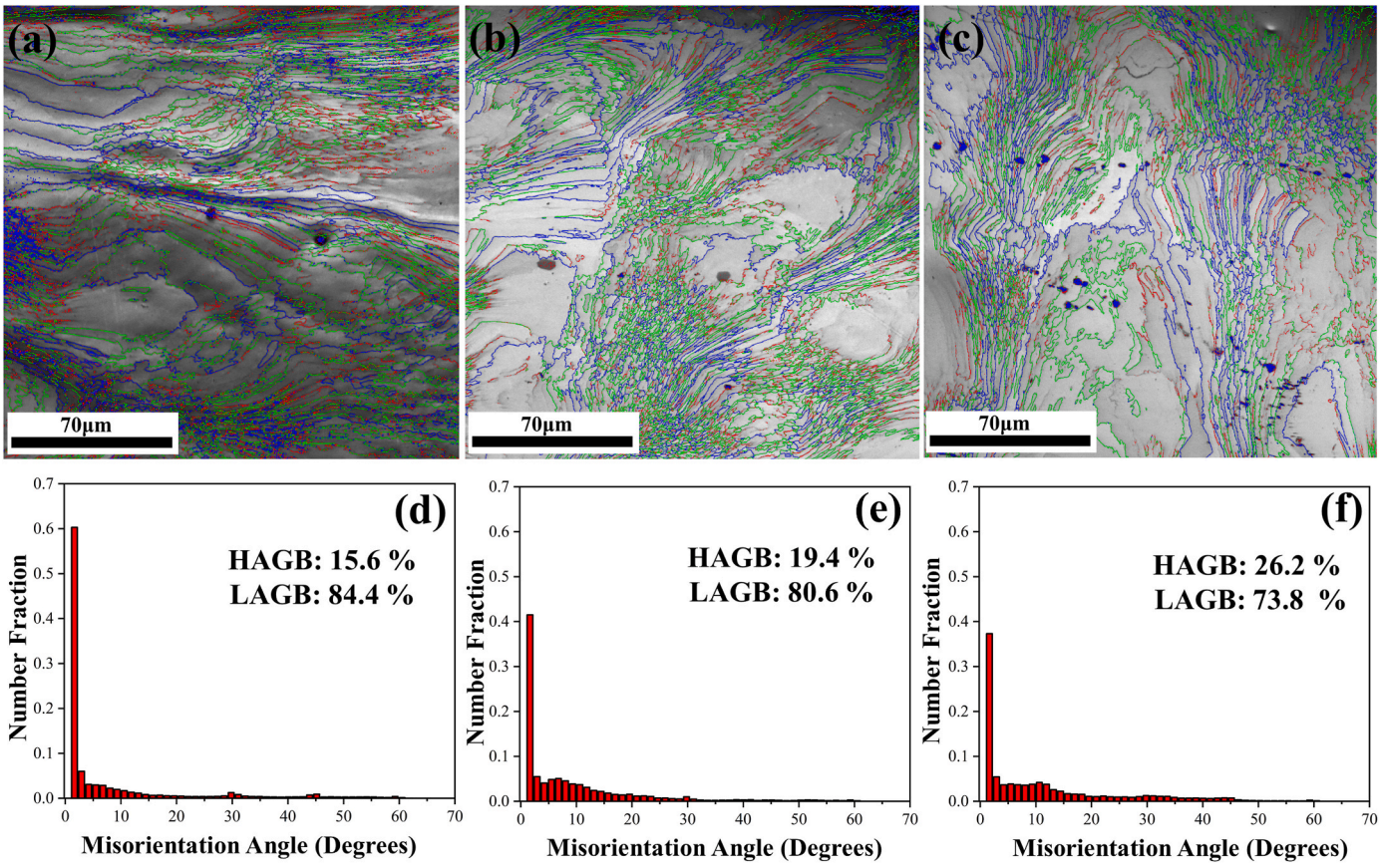

Fig. 9. The misorientation angle distributions of (a) C0, (b) C45, and (c) C90; HAGB statistics of (d) C0, (e) C45, and (f) C90.

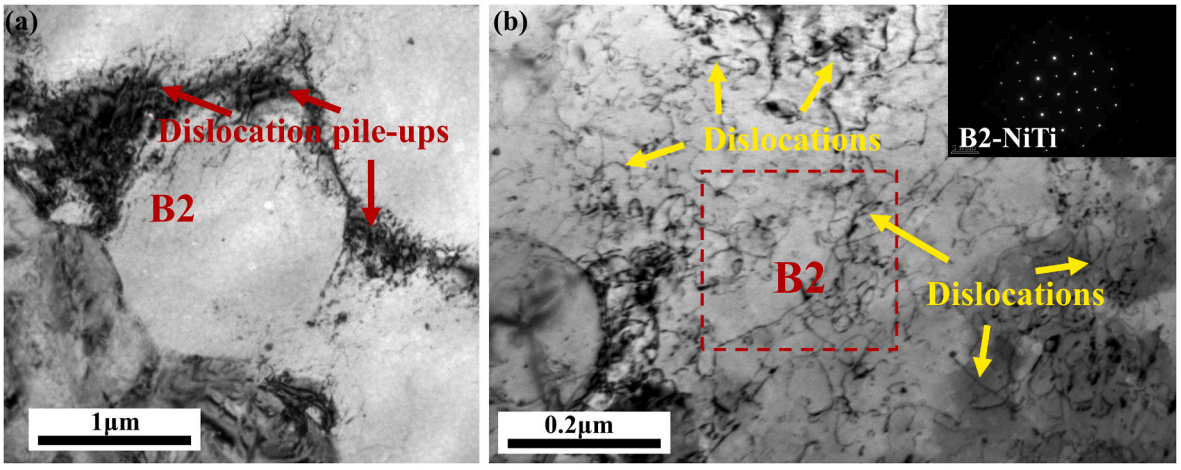

Fig. 10. TEM images of the fractured NiTi samples, (a) dislocations around the grain boundary; (b) A high magnification image of the dislocations and the corresponding selected area electron diffraction (SAED) image.

in comparison to the other samples [45].

The EBSD observations on the cross-sectional region perpendicular to the fracture surface of impact samples are conducted to further understand the effect of building directions on the impact properties.

Fig. 8 (a–c) show the distribution of GND density near the selected crack propagation region, which is performed to investigate the dislocation activities in each sample after the Charpy impact test. The GND density in sample C0 (Fig. 8 (a)) exhibits a relatively homogeneous distribution compared to the other samples. However, for sample C45, high GND densities are primarily concentrated at grain boundaries while intragranular GND densities are comparatively lower, as depicted in Fig. 8 (b). These were due to the hindrance of dislocation movement by grain boundaries, resulting in the formation of dislocation pile-ups and exhibiting macroscopic material plasticity, as shown in Fig. 10 (a). These observed characteristics demonstrate that C0 shows relatively uniform plastic deformation while C45 does not exhibit such behavior. Furthermore, the average number of GND densities in each sample is also calculated and presented in Fig. 8 (d)(e) and (f). Specifically, C0 displays a higher GND density of $0.89 \times 10^{12}/m^2$ compared to that measured for C45 and C90 which are recorded as $0.76 \times 10^{12}/m^2$ and

$0.66 \times 10^{12}/m^2$ respectively.

In General, there is a significant correlation between the deformation behavior of crystalline materials and the dislocation activities [46–48]. Specifically, the large mobility of dislocation can result in large plastic deformation, which can be reflected by the dislocation density [49]. During the deformation of crystalline materials, the dislocation activities usually require a large driving force, which could be supplied by dissipating impact energy. Consequently, samples with high GND density will consume more impact energy. Correspondingly, C0 shows the highest GND density among all the samples, indicating a stronger resistance to crack propagation.

Additionally, the findings from the GND density analysis are further validated through the examination of the KAM maps. As depicted in Fig. 8 (g–i), C0 shows a relatively homogeneous KAM map, while the color distributions (indicated by the green line) appear non-uniform in C45 and C90, reflecting that the high KAM values are mainly localized at the grain boundaries. Moreover, C0 (Fig. 8 (j)) exhibits a higher KAM value in comparison to both C45 (Fig. 8 (k)) and C90 (Fig. 8 (l)). The sequence is observed as follows: C0 > C45 >C90, implying a greater degree of plastic deformation in the case of C0.

Fig. 9 (a–c) display the misorientation angle distribution maps. Among them, the grain boundaries with the misorientation below 15° are defined as low angle grain boundaries (LAGB), which are denoted with the red and green lines. Those of misorientation greater than 15° are termed as HAGB and denoted by the blue line. The proportions of HAGB and LAGB are further quantified in Fig. 9 (d–f). As shown, the proportions of HAGB in C0, C45, and C90 are 15.6 %, 19.4 %, and 26.2 %, respectively, which shows an increasing trend. Among them, the proportion of HAGB in C0 is found to be the lowest compared to the others. Generally speaking, the presence of HAGB may impede the dislocation movement. In this case, these dislocations will accumulate in the grain boundaries during the impact loading, which may lead to the dislocations pile up. Finally, the stress concentration occurs along the grain boundaries, thereby facilitating crack propagation [10,50]. The plastic deformation capacity is hence deteriorated. As previously mentioned, the proportion of HAGB in C0 is minimal, thus minimizing their impact on material behavior. Therefore, C0 exhibits superior impact resistance properties.

Fig. 10 (b) shows a high-magnification image of the dislocations. It can be observed that the dislocations present wavy or bowed morphologies, which are consistent with those reported by Zhang et al. [38]. Furthermore, the corresponding SAED in the upper right corner exclusively reveals the presence of the austenite phase, suggesting that no phase transformation from austenite to martensite occurred during the impact loading process. According to several studies [51,52], this phenomenon has been attributed to the adiabatic effect. During the impact test, the samples undergo plastic deformation at a significantly higher strain rate (10^2-10^3 s^{-1}). In this case, heat conduction to the air was insufficient due to such rapid deformation [53,54]. As a result, the latent heat generated by the deformation significantly elevates the temperature of the samples. At this time, according to the Clausius-Clapeyron relationship [55], as the rise of the sample temperature increases, the critical stress for stress-induced martensite increases while the stress for slip decreases. When slip stress falls below the critical stress required for stress-induced martensite transformation, samples will undergo plastic deformation and fracture without undergoing stress-induced martensitic transformation.

4. Conclusion

In this paper, the impact properties of LPBFed NiTi SMAs with different building directions are first studied. It makes up the gap in the research on the impact properties of the LPBFed NiTi SMAs with a strain rate in the range of 10^2-10^3 s^{-1}. The main findings of this work are drawn as follows:

(1) The impact toughness of C0 is found to be superior when compared to that of C45 and C90. The texture orientation, the defects, and the relationship between the loading direction and the deposited layers play a crucial role.
(2) The building directions have no significant effect on the position of the phase transformation peaks but the width. Further heat treatment is expected to eliminate this difference. Moreover, there is no phase transformation behavior under the high-strain rate loading conditions due to the influence of the adiabatic effect.
(3) The impact toughness of LPBFed NiTi SMAs is poor. C0 has the best resistance to impact loading with a total impact absorbed energy of only 12.87 J. Further heat treatment should be done to improve the impact properties of LPBFed Niti SMA, like the aircraft structure materials, TC21 [56].

Declaration of competing interest

The authors declare that they have no known competing financial interests or personal relationships that could have appeared to influence the work reported in this paper.

Acknowledgments

This work was financially supported by the National Natural Science Foundation of China (Grant 52305302, 52025053, 52235006, 52105303) and the Natural Science Foundation of Jilin Province (Grant 20220101216JC).

References

[1] Miyazaki S. My Experience with Ti–Ni-Based and Ti-Based shape memory alloys. Shape Memory Superelast 2017;3:279–314. https://doi.org/10.1007/s40830-017-0122-3.
[2] Qiu P, Gao PP, Wang SY, Li ZH, Yang Y, Zhang QQ, Xiong ZW, Hao SJ. Study on corrosion behavior of the selective laser melted NiTi alloy with superior tensile property and shape memory effect. Corrosion Sci 2020;175:108891. https://doi.org/10.1016/j.corsci.2020.108891.
[3] Bagheri A, Mahtabi MJ, Shamsaei N. Fatigue behavior and cyclic deformation of additive manufactured NiTi. J Mater Process Technol 2018;252:440–53. https://doi.org/10.1016/j.jmatprotec.2017.10.006.
[4] Wang XB, Speirs M, Kustov S, Vrancken B, Li XB, Kruth JP, Humbeeck JV. Selective laser melting produced layer-structured NiTi shape memory alloys with high damping properties and Elinvar effect. Scripta Mater 2018;146:246–50. https://doi.org/10.1016/j.scriptamat.2017.11.047.
[5] Xu GX, Zheng LJ, Zhang FX, Zhang H. Influence of solution heat treatment on the microstructural evolution and mechanical behavior of 60NiTi. J Alloys Compd 2019;775:698–706. https://doi.org/10.1016/j.jallcom.2018.10.015.
[6] Wang Y, Aslani F, Valizadeh A. An investigation into the mechanical behaviour of fibre-reinforced geopolymer concrete incorporating NiTi shape memory alloy, steel and polypropylene fibres. Construct Build Mater 2020;259:119765. https://doi.org/10.1016/j.conbuildmat.2020.119765.
[7] Zhao M, Shao YM, Zheng WJ, Luo YH, Qiao JC, Wu SS, Yan YW, Guo W. Tailoring the damping and mechanical properties of porous NiTi by a phase leaching process. J Alloys Compd 2021;855:157471. https://doi.org/10.1016/j.jallcom.2020.157471.
[8] Wang X, Xu S, Zhou S, Xu W, Leary M, Choong P, Qian M, Brandt M, Xie YM. Topological design and additive manufacturing of porous metals for bone scaffolds and orthopaedic implants: a review. Biomaterials 2016;83:127–41. https://doi.org/10.1016/j.biomaterials.2016.01.012.
[9] Keshavarz MK, Sikan F, Boutet CE, Milligan J, Bois-Brochu A, Brochu M. Impact properties of half stress-relieved and hot isostatic pressed Ti-6Al-4V components fabricated by laser powder bed fusion. Mater Sci Eng, A 2019;760:481–8. https://doi.org/10.1016/j.msea.2019.05.035.
[10] Cui YH, Zeng XG, Tan VBC, Zhang ZL. Experimental and numerical studies of NiTi dynamic fracture behaviors under the impact loading. Int J Mech Sci 2022;235:107724. https://doi.org/10.1016/j.ijmecsci.2022.107724.
[11] Wang J, Ren XC, Xu YJ, Zhang WH, Zhu JH, Li B. Thermodynamic behavior of NiTi shape memory alloy against low-velocity impact: experiment and simulation. Int J Impact Eng 2020;139:103532. https://doi.org/10.1016/j.ijimpeng.2020.103532.
[12] Wang X, Xia WG, Wu XQ, Wei YP, Huang CG. Microstructure and mechanical properties of an austenite NiTi shape memory alloy treated with laser-induced shock. Mater Sci Eng, A 2013;578:1–5. https://doi.org/10.1016/j.msea.2013.04.058.
[13] Zhang XP, Wang GJ, Luo BQ, Bland SN, Tan F, Zhao F, Zhao JH, Sun CW, Liu CL. Mechanical response of near-equiatomic NiTi alloy at dynamic high pressure and

strain rate. J Alloys Compd 2018;731:569–76. https://doi.org/10.1016/j.jallcom.2017.10.080.
[14] Meo M, Marulo F, Guida M, Russo S. Shape memory alloy hybrid composites for improved impact properties for aeronautical applications. Compos Struct 2013;95:756–66. https://doi.org/10.1016/j.compstruct.2012.08.011.
[15] Hassan MR, Mehrpouya M, Dawood S. Review of the machining difficulties of Nickel-Titanium based shape memory alloys. Appl Mech Mater 2014;564:533–7. https://doi:10.4028/www.scientific.net/AMM.564.533.
[16] Jani JM, Leary M, Subic A, Gibson MA. A review of shape memory alloy research, applications and opportunities. Mater Des 2014;56:1078–113. https://doi.org/10.1016/j.matdes.2013.11.084.
[17] Gu DD, Meiners W, Wissenbach K, Poprawe R. Laser additive manufacturing of metallic components: materials, processes, and mechanisms. Int Mater Rev 2013;57(3):133–64. https://doi.org/10.1179/1743280411Y.0000000014.
[18] Sander G, Babu AP, Gao X, Jiang D, Birbilis N. On the effect of build orientation and residual stress on the corrosion of 316L stainless steel prepared by selective laser melting. Corrosion Sci 2021;179:109149. https://doi.org/10.1016/j.corsci.2020.109149.
[19] Sanjari M, Mahmoudiniya M, Pirgazi H, Tamimi S, Ghoncheh MH, Shahriairi A, Hadadzadeh A, Amirkhiz BS, Purdy M, de Araujo EG, Kestens L, Mohammadi M. Microstructure, texture, and anisotropic mechanical behavior of selective laser melted maraging stainless steels. Mater Char 2022;192:112185. https://doi.org/10.1016/j.matchar.2022.112185.
[20] Moghaddam NS, Saghaian SE, Amerinatanzi A, Ibrahim H, Li PZ, Toker GP, Karaca HE, Elahinia M. Anisotropic tensile and actuation properties of NiTi fabricated with selective laser melting. Mater Sci Eng, A 2018;724:220–30. https://doi.org/10.1016/j.msea.2018.03.072.
[21] Nematollahi M, Saghaian SE, Safaei K, Bayati P, Bassani P, Biffi C, Tuissi A, Karaca H, Elahinia M. Building orientation-structure-property in laser powder bed fusion of NiTi shape memory alloy. J Alloys Compd 2021;873:159791. https://doi.org/10.1016/j.jallcom.2021.159791.
[22] Bayati P, Jahadakbar A, Barati M, Nematollahi M, Saint-Sulpice L, Haghshenas M, Chirani SA, Mahtabi MJ, Elahinia M. Toward low and high cycle fatigue behavior of SLM-fabricated NiTi: considering the effect of build orientation and employing a self-heating approach. Int J Mech Sci 2020;185:105878. https://doi.org/10.1016/j.ijmecsci.2020.105878.
[23] Safaei K, Nematollahi M, Bayati P, Kordizadeh F, Andani MT, Abedi H, Poorganji B, Elahinia M. On the crystallographic texture and torsional behavior of NiTi shape memory alloy processed by laser powder bed fusion: effect of build orientation. Addit Manuf 2022;59:103184. https://doi.org/10.1016/j.addma.2022.103184.
[24] Zhang XL, Jiang Y, Wang SP, Wang S, Wang ZQ, Yu ZL, Zhang ZH, Ren LQ. Compression behavior and failure mechanisms of bionic porous NiTi structures built via selective laser melting. Acta Metallurgica Sinica-English Lett 2023;36:926–36. https://doi.org/10.1007/s40195-023-01523-w.
[25] Lucon E. Experimental assessment of the equivalent strain rate for an instrumented Charpy Test. J Res Natl Instit Stand Technol 2016;121. https://doi.org/10.6028/jres.121.007.
[26] Meier H, Haberland C, Frenzel J. Structural and functional properties of NiTi shape memory alloys produced by Selective Laser Melting. Innovative developments in virtual and physical prototyping. 2012. p. 291–6. http://doi:10.1201/b11341-47.
[27] Dadbakhsh S, Speirs M, Kruth JP, Schrooten J, Luyten J, Van Humbeeck J. Effect of SLM parameters on transformation temperatures of shape memory Nickel Titanium parts. Adv Eng Mater 2014;16(9):1140–6. https://doi.org/10.1002/adem.201300558.
[28] Speirs M, Wang XB, Van Baelen S, Ahadi A, Dadbakhsh S, Kruth JP, Van Humbeeck J. On the transformation behavior of NiTi Shape-Memory alloy produced by SLM. Shape Memory Superelast 2016;2(4):310–6. https://doi.org/10.1007/s40830-016-0083-y.
[29] Krishna BV, Bose S, Bandyopadhyay A. Laser processing of net-shape NiTi shape memory alloy. Metall Mater Trans 2007;38A(5):1096–103. https://doi.org/10.1007/s11661-007-9127-4.
[30] Meng QL, Yang H, Liu YN, Nam TH. Transformation intervals and elastic strain energies of B2-B19' martensitic transformation of NiTi. Intermetallics 2010;18(12):2431–4. https://doi.org/10.1016/j.intermet.2010.08.038.
[31] Wang XB, Yu JY, Liu JW, Chen LG, Yang Q, Wei HL, Sun J, Wang ZC, Zhang ZH, Zhao GQ, Van Humbeeck J. Effect of process parameters on the phase transformation behavior and tensile properties of NiTi shape memory alloys fabricated by selective laser melting. Addit Manuf 2020;36:101545. https://doi.org/10.1016/j.addma.2020.101545.
[32] Ma J, Franco B, Tapia G, Karayagiz K, Johnson L, Liu J, Arroyave R, Karaman I, Elwany A. Spatial control of functional response in 4D-printed active metallic structures. Sci Rep 2017;7:46707. https://doi.org/10.1038/srep46707.
[33] Marattukalam JJ, Balla VK, Das M, Bontha S, Kalpathy SK. Effect of heat treatment on microstructure, corrosion, and shape memory characteristics of laser deposited NiTi alloy. J Alloys Compd 2018;744:337–46. https://doi.org/10.1016/j.jallcom.2018.01.174.
[34] Mohamed EMA, Zou J, Sheridan RS, Bongs K, Attallah MM. Magnetic shielding promotion via the control of magnetic anisotropy and thermal post processing in laser powder bed fusion processed NiFeMo-based soft magnet. Addit Manuf 2020;32:101079. https://doi.org/10.1016/j.addma.2020.101079.
[35] Hadadzadeh A, Ainirkhiz BS, Li J, Mohammadi M. Columnar to equiaxed transition during direct metal laser sintering of AlSi10Mg alloy: effect of building direction. Addit Manuf 2018;23:121–31. https://doi.org/10.1016/j.addma.2018.08.001.
[36] Zhou Q, Hayat MD, Chen G, Cai S, Qu XH, Tang HP, Cao P. Selective electron beam melting of NiTi: microstructure, phase transformation and mechanical properties. Mater Sci Eng, A 2019;744:290–8. https://doi.org/10.1016/j.msea.2018.12.023.
[37] Dehgahi S, Ghoncheh MH, Hadadzadeh A, Sanjari M, Amirkhiz BS, Mohammadi M. The role of titanium on the microstructure and mechanical properties of additively manufactured C300 maraging steels. Mater Des 2020;194:108965. https://doi.org/10.1016/j.matdes.2020.108965.
[38] Zhang QQ, Hao SJ, Liu YT, Xiong ZW, Guo WQ, Yang Y, Ren Y, Cui LS, Ren LQ, Zhang ZH. The microstructure of a selective laser melting (SLM)-fabricated NiTi shape memory alloy with superior tensile property and shape memory recoverability. Appl Mater Today 2020;19:100547. https://doi.org/10.1016/j.apmt.2019.100547.
[39] Sun SH, Hagihara K, Ishimoto T, Suganuma R, Xue YF, Nakano T. Comparison of microstructure, crystallographic texture, and mechanical properties in Ti-15Mo-5Zr-3Al alloys fabricated via electron and laser beam powder bed fusion technologies. Addit Manuf 2021;47:102329. https://doi.org/10.1016/j.addma.2021.102329.
[40] Tanguy B, Besson J, Piques R, Pineau A. Ductile to brittle transition of an A508 steel characterized by Charpy impact test - Part II: modeling of the Charpy transition curve. Eng Fract Mech 2005;72(3):413–34. https://doi.org/10.1016/j.engfracmech.2004.03.010.
[41] Shin HS, Tuazon BJ. An instrumented drop-bar impact testing apparatus for investigating the impact fracture behaviors of structural steels. Int J Impact Eng 2015;84:124–33. https://doi.org/10.1016/j.ijimpeng.2015.05.017.
[42] Wang P, Lu SP, Xiao NM, Li DZ, Li YY. Effect of delta ferrite on impact properties of low carbon 13Cr-4Ni martensitic stainless steel. Mater Sci Eng, A 2010;527(13–14):3210–6. https://doi.org/10.1016/j.msea.2010.01.085.
[43] Yoon KB, Dao VH, Yu JM. Effects of build direction on tensile and creep properties of 316L stainless steel produced by selective laser melting. Fatig Fract Eng Mater Struct 2020;43(11):2623–36. https://doi.org/10.1111/ffe.13322.
[44] Wu MW, Lai PH, Chen JK. Anisotropy in the impact toughness of selective laser melted Ti-6Al-4V alloy. Mater Sci Eng, A 2016;650:295–9. https://doi.org/10.1016/j.msea.2015.10.045.
[45] Moghaddama NS, Saghaianb SE, Anerinatanzia A, Ibrahima H, Lib P, Tokerb GP, Karacab HE, Elahiniaa M. Anisotropic tensile and actuation properties of NiTi fabricated with Selective Laser Melting. Mater Sci Eng, A 2018;724:220–30. https://doi.org/10.1016/j.msea.2018.03.072.
[46] Kale C, Garg P, Bazehhour BG, Srinivasan S, Bhatia MA, Peralta P, Solanki KN. Oxygen effects on crystal plasticity of Titanium: a multiscale calibration and validation framework. Acta Mater 2019;176:19–32. https://doi.org/10.1016/j.actamat.2019.06.040.
[47] Huang SX, Zhao QY, Zhao YQ, Lin C, Wu C, Jia WJ, Mao CL, Ji V. Toughening effects of Mo and Nb addition on impact toughness and crack resistance of titanium alloys. J Mater Sci Technol 2021;79:147–64. https://doi.org/10.1016/j.jmst.2020.11.045.
[48] Tanguy D, Razafindrazaka M, Delafosse D. Multiscale simulation of crack tip shielding by a dislocation. Acta Mater 2008;56(11):2441–9. https://doi.org/10.1016/j.actamat.2008.01.031.
[49] Gavriljuk VG, Shivanyuk VN, Shanina BD. Change in the electron structure caused by C, N and H atoms in iron and its effect on their interaction with dislocations. Acta Mater 2005;53(19):5017–24. https://doi.org/10.1016/j.actamat.2005.07.028.
[50] Long SL, Liang YL, Jiang Y, Liang Y, Yang M, Yi YL. Effect of quenching temperature on martensite multi-level microstructures and properties of strength and toughness in 20CrNi2Mo steel. Mater Sci Eng, A 2016;676:38–47. https://doi.org/10.1016/j.msea.2016.08.065.
[51] Madivala M, Bleck W. Strain Rate Dependent mechanical properties of TWIP steel. Jom 2019;71(4):1291–302. https://doi.org/10.1007/s11837-018-3137-0.
[52] Bragov A, Igumnov L, Konstantinov A, Lomunov A, Rusin E. Effects of high strain rate and self-heating on plastic deformation of metal materials under fast compression loading. J Dyn Behav Mater 2019;5(3):309–19. https://doi.org/10.1007/s40870-019-00214-x.
[53] Zhang XH, Feng P, He YJ, Yu TX, Sun QP. Experimental study on rate dependence of macroscopic domain and stress hysteresis in NiTi shape memory alloy strips. Int J Mech Sci 2010;52:1660–70. https://doi:10.1016/j.ijmecsci.2010.08.007.
[54] Elibol C, Wagner FX. Strain Rate Effects on the localization of the stress-induced Martensitic transformation in pseudoelastic NiTi under uniaxial tension, compression and compression–shear. Mater Sci Eng, A 2015;643:194–202. https://doi:10.1016/j.msea.2015.07.039.
[55] Otsuka K, Ren XB. Physical metallurgy of Ti-Ni-based shape memory alloys. Prog Mater Sci 2005;50(5):511–678. https://doi.org/10.1016/j.pmatsci.2004.10.001.
[56] Lei L, Zhao QY, Zhao YQ, Huang SX, Wu C, Jia WJ, Zeng WD. Study on the intrinsic factors determining impact toughness of TC21 alloy. Mater Char 2021;177:111164. https://doi.org/10.1016/j.matchar.2021.111164.